



## Enhanced photocatalytic ozonation of organic pollutants using an iron-based metal-organic framework

Deyou Yu<sup>a,b</sup>, Lubiao Li<sup>a,b</sup>, Minghua Wu<sup>a,b,\*</sup>, John C. Crittenden<sup>c</sup>

<sup>a</sup> Engineering Research Center for Eco-Dyeing and Finishing of Textiles, Ministry of Education, Zhejiang Sci-Tech University, Hangzhou 310018, PR China

<sup>b</sup> Key Laboratory of Advanced Textile Materials & Manufacturing Technology, Ministry of Education, Zhejiang Sci-Tech University, Hangzhou 310018, PR China

<sup>c</sup> Brook Byers Institute for Sustainable Systems, School of Civil and Environmental Engineering, Georgia Institute of Technology, Atlanta, Georgia 30332, United States



### ARTICLE INFO

#### Keywords:

Photocatalytic ozonation  
Lewis acid sites  
Metal-organic frameworks  
Synergistic effect  
Reactive oxygen species

### ABSTRACT

The photocatalytic activity of metal-organic frameworks (MOFs) is drawing great attention in the field of environmental remediation. However, the efficiency of MOFs still remains low because of the rapid recombination of valence band holes and conduction band electrons (a.k.a., charge carriers). The combination of photocatalysis and electron acceptors such as ozone are believed to be an efficient strategy to reduce the charge carrier recombination. Herein, we report that photocatalytic ozonation (PCO) using an Fe-based MOF (MIL-88A(Fe)) has greater destruction than photocatalysis and/or catalytic ozonation in terms of 4-nitrophenol (4-NP) degradation and mineralization. It is worth noting that our Fe-based MOF has a large number of Lewis acid sites (LAS). The pseudo-first order kinetic rate constants (*k*) of 4-NP degradation using PCO, photocatalysis and catalytic ozonation systems are 0.1632, 0.0143 and 0.0840 min<sup>-1</sup>, respectively. The TOC removal of 4-NP in the PCO system is approximately 75.4% ([4-NP] = 100 ppm, ozone input dosage = 1.5 mg/min·L, UV light intensity = 3.46 × 10<sup>-6</sup> Einstiens/L·s, treatment time = 30 min) and this is much greater than those of photocatalysis (17.6%) and catalytic ozonation (38.7%). Most importantly, both the *k* value and TOC removal in the PCO system are much higher than the sum of those in other two processes, implying a strong synergistic effect in the PCO process. Mechanistic studies were conducted using electrochemical impedance spectroscopy (EIS) and photoluminescence (PL) measurements and demonstrate that the synergistic effect may originate from the enhanced photoinduced carrier separation using ozone as an electron acceptor. Furthermore, ·OH, ·O<sub>2</sub><sup>-</sup>, and <sup>1</sup>O<sub>2</sub> are found to be the principal reactive oxygen species (ROS) for 4-NP degradation and mineralization. Integrating the analysis of band structure, EPR and scavenging experiment results, ozone is not only able to reduce charge carrier recombination but also can be catalytically decomposed to generate more ROS on the LAS of MIL-88A(Fe). This study provides deep insights into the use of MOFs as effective advanced oxidation processes (AOPs).

### 1. Introduction

Advanced oxidation processes (AOPs) are effective for destroying organic pollutants in aqueous solution [1–6]. The efficiency of AOPs like catalytic ozonation and photocatalysis may be significantly improved by combining them. Organic pollutant mineralization and ozone utilization in catalytic ozonation can be improved [7–11]. The swift recombination of photogenerated carriers in photocatalysis seems to be reduced by adding ozone [12–20]. Accordingly, the combining catalytic ozonation and photocatalysis may prove to be a more effective treatment process.

Photocatalytic ozonation (PCO), which combines photocatalysis and

ozonation, is a promising technology for the efficient destruction of organic pollutants [21–23]. PCO has following advantages: (1) ozone can scavenge conduction band electrons (e<sup>-</sup>) and reduce charge carrier recombination and (2) ozone can react with the catalyst to produce additional ROS. These two factors increase the effectiveness of photocatalysis and ozonation.

Iron-based metal-organic frameworks (Fe-MOFs), constructed of iron-oxo clusters and organic linkers, have triggered significant interest in photocatalytic water treatment [15,24–29]. Laurier et al. demonstrated the remarkable photocatalytic activity of MIL-88B(Fe), MIL-100(Fe) and MIL-101(Fe) for rhodamine 6 G degradation for the first time [30]. Afterwards, Wu et al. reported that MIL-53(Fe) and MIL-

\* Corresponding author at: Engineering Research Center for Eco-Dyeing and Finishing of Textiles, Ministry of Education, Zhejiang Sci-Tech University, Hangzhou 310018, PR China.

E-mail address: [wmh@zstu.edu.cn](mailto:wmh@zstu.edu.cn) (M. Wu).

68(Fe) were efficient photocatalysts for simultaneous Cr(VI) reduction and dye oxidation [14,31]. Furthermore, the rapid destruction of tetracycline was observed with Fe-MOFs (i.e., MIL-53(Fe), MIL-100(Fe), and MIL-101(Fe)) and this was attributed to simultaneous adsorption and photocatalysis [32]. Despite these advances, the total photocatalytic efficiency is still limited by the rapid recombination of photogenerated charge carriers.

To overcome this shortcoming, three strategies have been developed recently: (1) fabrication of Fe-MOFs based heterojunctions [24,33–35]; (2) band gap engineering using electron-donating or accepting groups (e.g., –OH, –NH<sub>2</sub>, –COOH, –NO<sub>2</sub> and –H) [36,37]; (3) introduction of electron acceptors using H<sub>2</sub>O<sub>2</sub> and persulfate [38,39]. Among them, the third strategy is the most promising scenario for reducing the charge carrier recombination because it is easy to implement and it improves the quantum yield. Hydrogen peroxide ( $E^{\circ} = 1.77$  V) and persulfate ( $E^{\circ} = 2.01$  V) are two widely used electron acceptors in Fe-MOFs based photocatalytic systems. The oxidants can scavenge photogenerated electrons to reduce electron-hole recombination, and this results in higher organic pollution degradation. Unfortunately, the enhancements in degradation are still small. Accordingly, we have explored the use of electron acceptors that have a larger reduction potential.

Compared to H<sub>2</sub>O<sub>2</sub> and persulfate, ozone is a much more powerful scavenger of electrons due to its higher redox potential ( $E^{\circ} = 2.07$  V), and it may capture conduction band electrons more effectively. In addition, we found that Fe-MOFs have a high concentration of Lewis acid surface sites and they effectively decompose ozone into ROS to increase the organic compound destruction [40]. Accordingly, combining Fe-MOFs for photocatalysis and catalytic ozonation decomposition is a promising technique for increased organic compound degradation and mineralization.

In this study, we report the PCO performance using MIL-88A(Fe) to degrade 4-nitrophenol (4-NP). The synergistic effect of photocatalysis and ozonation was quantitatively evaluated. The influence of initial pH value on 4-NP degradation during the PCO procedure was also investigated. Radical quenching experiments and EPR techniques were performed to clarify the role of ROS in 4-NP degradation. Furthermore, the role of ozone was quantified. Finally, the PCO mechanism of 4-NP by MIL-88A(Fe) is proposed. This study provides deep insights into the exploration of MOFs as effective AOPs.

## 2. Experimental section

### 2.1. Chemicals

Iron chloride hexahydrate (FeCl<sub>3</sub>·6H<sub>2</sub>O), fumaric acid (FA), 4-nitrophenol (4-NP), sodium thiosulfate pentahydrate (Na<sub>2</sub>S<sub>2</sub>O<sub>3</sub>·5H<sub>2</sub>O), sodium chloride (NaCl), trisodium phosphate (Na<sub>3</sub>PO<sub>4</sub>), isopropanol (IPA), p-benzoquinone (BQ), sodium azide (NaN<sub>3</sub>), 5,5-dimethyl-pyrrole-N-oxide (DMPO), 4-amino-2,2,6,6-tetramethylpiperidine (TEMP) and other chemicals were purchased from Aladdin Chemical Co., Ltd. All chemicals were of analytical grade and used as received. Commercial P25 was purchased from Guangzhou Heqian Trading Co., Ltd. Ultrapure-water (UPW) employed was produced using a Milli-Q Advantage A10 (Millipore).

### 2.2. Preparation of MIL-88A(Fe)

MIL-88A(Fe) was synthesized using a facile hydrothermal method according to a previous study with some modifications [41]. A precursor solution was prepared by adding FeCl<sub>3</sub>·6H<sub>2</sub>O (20 mmol) and fumaric acid (20 mmol) into 150 mL UPW at 60 °C, and then it was transferred into an autoclave in a Teflon reactor (200 mL). The FA couldn't be completely dissolved at room temperature; consequently, the autoclave was kept at 65 °C for 12 h to crystallize and then the suspension was left to cool naturally. Afterwards, a solid powder was obtained by centrifugation (RCF = 10,619 × g, 5 min), and then the

powder was washed with hot ethanol (60 °C) and UPW to remove residual impurities. Finally, the brown-red product was dried in a vacuum oven at 100 °C for 24 h.

### 2.3. Characterizations and measurements

The powder X-ray diffraction (PXRD) patterns were measured using a diffractometer (D8 discover, Bruker, 2θ = 3–50°). A Fourier transform-infrared (FTIR) spectrometer (Vertex 70, Bruker, resolution = 4 cm<sup>-1</sup>) was used to measure the FTIR spectra of samples. The MIL-88A(Fe) morphology was analyzed using a scanning electron microscope (SEM, Ultra 55, Zeiss, EHT = 1.5 kV). The elemental analysis was performed by an SEM equipped energy dispersive X-ray spectroscopy (EDS, X-Max<sup>N</sup>, Oxford Instrument, EHT = 10 kV). The pore size distribution and surface area were determined from a N<sub>2</sub> adsorption-desorption isotherm using the automated gas adsorption system (ASAP 2020, Micromeritics). X-ray photoelectron spectroscopy (XPS, K-Alpha, Thermo) was used to determine the elemental composition and electronic structure. The UV-vis diffuse reflectance spectra were obtained using a UV-2600 UV-vis spectrometer (SHIMADZU, Japan) for wavelengths from 300 to 800 nm. PL spectra of catalyst suspensions (0.2 g/L) with and without ozone were measured using a fluorescence spectrophotometer (F-4600, HITACHI) with an excitation wavelength of 320 nm. The EIS and M-S spectra were measured using electrochemical experiments and they were performed on an electrochemical workstation (CHI660D Apparatuses). Detailed information containing electrode preparation and testing conditions of electrochemical impedance spectroscopy (EIS) and Mott-Schottky (M-S) measurements are provided in the Supporting Information (SI).

### 2.4. PCO procedure

The PCO degradation was examined using 4-NP as a model compound. The experimental setup of PCO is shown in Fig. S1. Generally, degradation experiments were conducted in completely mixed batch reactor. Two UV lamps (Philips, TUV 6 W, 254 nm) surrounded the reactor when photocatalytic experiments were conducted. The initial 4-NP concentration was 100 ppm unless stated otherwise. The initial pH value was adjusted using HCl or NaOH solutions. In a typical PCO procedure, 500 mL 4-NP aqueous solution and 50 mg MIL-88A(Fe) were transferred to the reactor. At the beginning of the experiment, a 30 mg/L ozone stream, produced from an ozone generator (Tonglin Technology 3S-T3, using high purity O<sub>2</sub>), was bubbled into the bottle of the reactor using an aerator with a 25 mL/min flow rate (ozone input dosage = 1.5 mg/min-L). At given time intervals, about 5.0 mL sample was withdrawn and placed into a centrifuge tube for analysis after it was filtered using a 0.45 μm microfilter. After sampling the residual ROS and O<sub>3</sub> were eliminated by adding 2 drops of 0.1 mol/L Na<sub>2</sub>S<sub>2</sub>O<sub>3</sub> solution. Adsorption, ozonation alone, photocatalysis alone, catalytic ozonation and photolysis (without MIL-88A(Fe)) were also performed under equivalent conditions.

### 2.5. Analysis methods

The UV light intensity was measured according to a ferrioxalate actinometry method [42]. The 4-NP concentration was determined using high performance liquid chromatography (HPLC, Agilent Technologies Series 1260) with a UV-vis detector (Waters 2489) at 320 nm. A ZORBAX Eclipse XDB-C18 column (3.5 μm, 4.6 × 150 mm) was used as the stationary phase and maintained at 30 °C. A mixture of 2 mM H<sub>3</sub>PO<sub>4</sub> aqueous solution (30%) and methanol (70%) was used as the mobile phase and the flow rate was 0.75 mL/min. Under these conditions, the retention time was about 2.87 min. The electrical energy per order (EE/O) in terms of 4-NP removal efficiency and TOC removal was calculated according to a previous report [43]. The total organic carbon (TOC) was measured using a TOC analyzer (Elementar, Liquid). The

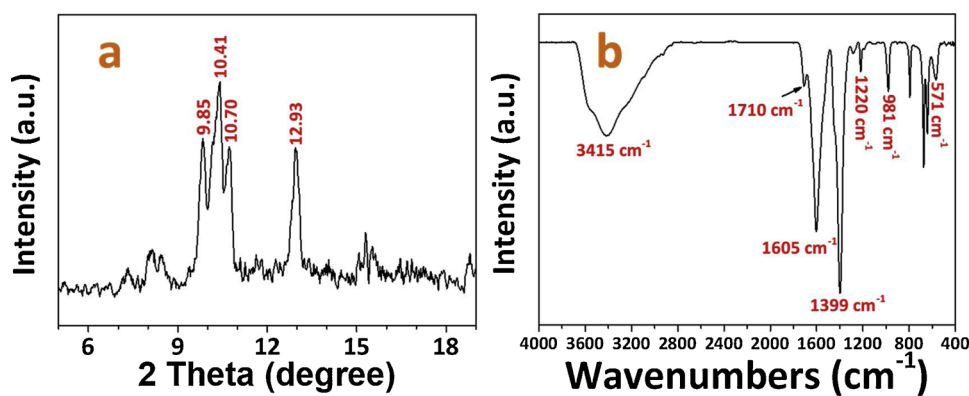


Fig. 1. XRD pattern (a) and FTIR spectrum (b) of MIL-88A(Fe).

ROS were measured using conventional radical quenching experiments and EPR techniques. For the conventional radical quenching experiments, IPA, BQ and NaN<sub>3</sub> were employed to trap ·OH, ·O<sub>2</sub><sup>−</sup> and <sup>1</sup>O<sub>2</sub>, respectively. The EPR spectra were recorded on a Bruker A300 spectrometer using DMPO and TEMP as radical trapping agents at room temperature. The iron leaching during PCO and the iron content in bulk MIL-88A(Fe) (after digestion) were determined by an inductively coupled plasma optical emission spectrometer (ICP-OES, Agilent 720). The intermediates that were formed during 4-NP degradation were identified by time-of-flight mass spectrometry (ToF-MS, SYNAPT G2-S, Waters) in the negative ion mode.

### 3. Results and discussion

#### 3.1. Characterizations

The crystal structure of MIL-88A(Fe) was characterized by PXRD and the result is presented in Fig. 1a. MIL-88A(Fe) displays four main peaks at the  $2\theta = 9.85^\circ$ ,  $10.41^\circ$ ,  $10.70^\circ$  and  $12.93^\circ$ , which agree well with a previous report (see Fig. S2) and show a fine-developed ordered structure [44]. The FTIR spectrum in Fig. 1b reveals the chemical structure of MIL-88A(Fe). The vibrations of C=O group are detected at peaks of  $1710$ ,  $1605$  and  $1399$   $\text{cm}^{-1}$  [39,41]. A broad peak at  $3415$   $\text{cm}^{-1}$  is ascribed to water molecules and this is due to the water adsorption of MIL-88A(Fe). The characteristic peaks at  $1220$ ,  $981$  and  $571$   $\text{cm}^{-1}$  are assigned to the stretching vibration of C–C, the bending vibration of C–H in trans-diene and the stretching vibration of Fe–O, respectively [3,39]. As observed in Fig. 2a and 2b, MIL-88A(Fe) has a uniform needle-shaped morphology (about  $0.6 \times 2 \mu\text{m}$ ) with a regular hexahedron in the middle part. The EDS spectrum (Fig. 2c) suggests the presence of C, O, Fe and also trace Cl elements. In addition, the iron content in bulk MIL-88A(Fe) is  $225.6 \text{ mg/g}$  and equals to  $22.56 \text{ wt\%}$ . A type-IV  $\text{N}_2$  isotherm with an H3 loop ( $P/P_0 = 0.5–1.0$ ) is found in Fig. 2d and this indicates a mesoporous structure for MIL-88A(Fe) [45]. The porous properties including the specific surface area (SSA), pore volume (PV) and average pore size (APS) of MIL-88A(Fe) are calculated to be  $19.74 \text{ m}^2/\text{g}$ ,  $0.03703 \text{ cm}^3/\text{g}$  ( $\text{PS} < 353.2 \text{ nm}$ ) and  $7.50 \text{ nm}$ , respectively, from the  $\text{N}_2$  sorption-desorption isotherm (inset in Fig. 2d) using Brunauer–Emmett–Teller (BET) method. The pore structure of MIL-88A(Fe) is very similar to the Liu's study [37], suggesting its successful fabrication.

XPS measurements were conducted to further investigate the element composition and chemical environment of MIL-88A(Fe). It can be observed from the survey spectrum (Fig. 3a) that C, O and Fe are main elements in MIL-88A(Fe), which agrees well with the EDS result. The binding energies (BEs) of  $284.8$  and  $289.2 \text{ eV}$  in the C 1s spectrum (Fig. 3b) are individually ascribed to C=C and C=O [31]. For the O 1s spectrum in Fig. 3c, the deconvolution peaks at  $532.1$  and  $532.9 \text{ eV}$  can be ascribed to O–Fe of the nodes and O=C of the linkers,

respectively [46]. Fig. 3d illustrates the high-resolution XPS spectrum of Fe 2p. Two main peaks at BE =  $712.1$  and  $726.0 \text{ eV}$  accompanied by another peak (BE =  $716.5 \text{ eV}$ ) correspond to Fe 2p<sub>3/2</sub> and Fe 2p<sub>1/2</sub>, respectively. Together with the peak distance ( $13.9 \text{ eV}$ ) that similar to  $\alpha\text{-Fe}_2\text{O}_3$ , Fe(III) can be identified as the main component in MIL-88A(Fe). Therefore, these results further verify the successful synthesis of MIL-88A(Fe).

The optical properties of MIL-88A(Fe) were tested by UV-vis DRS, as illustrated in Fig. 4a. The FA linker in MIL-88A(Fe) most likely generate photoelectrons via UV excitation due to its strong absorbance at a wavelength of around  $300 \text{ nm}$ . After photoelectron production, the ligand-to-metal-charge-transfer (LMCT) occurs for emerging photocatalytic applications [47–49]. Compared to FA, MIL-88A(Fe) exhibits an enhanced light absorbency in a wide range from  $300$  to  $800 \text{ nm}$ . The observed band at  $300$ – $600 \text{ nm}$  is caused by the  $[{}^6\text{A}_{1g} = > {}^4\text{A}_{1g} + {}^4\text{E}_g(\text{G})]$  transition of Fe(III) in MIL-88A(Fe) [50,51]. By plotting the tangent, as shown in Fig. 4b, the band gap of MIL-88A(Fe) is determined to be  $2.60 \text{ eV}$  according to the intercept, which matches well with a previous study [41]. The results suggest that MIL-88A(Fe) is expected to be a photocatalyst. In addition, the conduction and valence bands are further analyzed via mechanism investigation with M–S and valence XPS measurements.

It is believed that the Lewis acid sites (LAS) are significant active components in the catalytic ozonation [52]. Py-FTIR analysis allows us to determine the type and amount of acid sites according to previous reports [53,54]. Fig. 5 displays the Py-FTIR spectra of MIL-88A(Fe) at different degassing temperatures. Three clear peaks at about  $1070$ ,  $1042$  and  $1012 \text{ cm}^{-1}$  are found and they correspond to the typical vibration modes ( $v_{18a}$ ,  $v_{12}$  and  $v_1$ ) of LAS after pyridine sorption [53,54]. The peak intensity decays with increasing temperature and almost become zero at  $250^\circ\text{C}$ , which implies that there are only a few strong LAS in the MIL-88A(Fe). To quantify the amount of various LAS, the peak area of  $1070 \text{ cm}^{-1}$  was calculated. According to Volkringer et al. [53] and Emeis et al. [55], the Lewis acidity (LA) was determined using a value of  $0.6 \text{ cm}/\mu\text{mol}$  as the molar absorption coefficient, which is summarized in Table 1. Therefore, the amount of total, medium and strong LAS is estimated to be  $8.53$ ,  $4.42$  and  $0.79 \text{ mmol/g}$ , respectively. Moreover, in terms of total and medium sites, it is about  $9$  and  $6$  times higher than those in Bing's work, they found that their  $\gamma\text{-Ti-Al}_2\text{O}_3$  catalyst had a high efficiency regarding to organic destruction rate and TOC removal [52]. Together with the photoresponse result from UV-vis DRS analysis, it is reasonable to deduce that MIL-88A(Fe) is also an efficient catalyst for PCO.

#### 3.2. PCO activity

There are six degradation systems including photolysis (only UV light), photocatalysis (UV + catalyst or Vis light + catalyst), ozonation alone (only ozone), catalytic ozonation (ozone + catalyst), UV/ozone

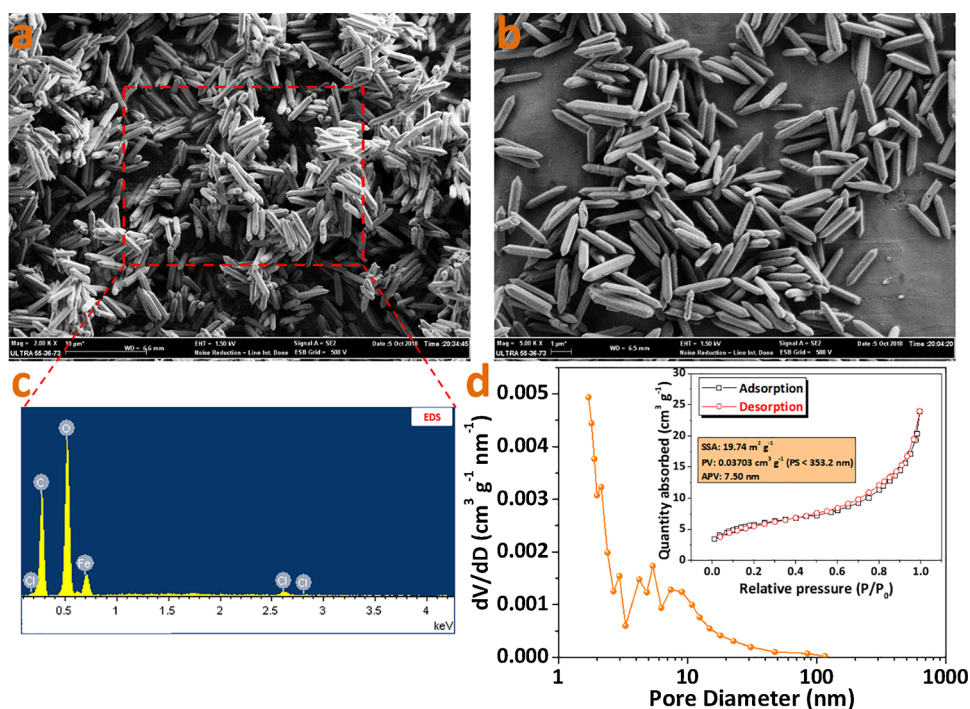


Fig. 2. SEM images (a, b), EDS spectrum (c) and N<sub>2</sub> adsorption-desorption isotherm (d) (Inset is the pore size distribution) of MIL-88A(Fe).

(UV + ozone) and PCO (UV + ozone + catalyst). We analyzed and discussed the data followed this order. The photocatalysis represents the degradation of 4-NP in [UV + catalyst] or [Vis light + catalyst] system. Only UV or Vis light is added. It not includes the ozone.

The PCO activity of MIL-88A(Fe) was examined by oxidizing 4-NP in aqueous solution. At 30 min, 6.9% 4-NP is absorbed into MIL-88A(Fe) without UV light and ozone addition (Fig. 6a and d, Table S1), and this means it increases the 4-NP on the surface and this increases the degradation rate. Almost no degradation of 4-NP is observed with

UV (254 nm) alone and about 33.6% 4-NP is removed with UV light and the MIL-88A(Fe) catalyst after 30 min (Fig. 6a and d, Table S1). This photocatalytic performance is similar to Liu et al. [41]. However, the efficiency is unsatisfactory and this is due to its rapid charge carrier recombination. Since there is trace Cl<sup>-</sup> ions present (about 1.2 wt%) in MIL-88A(Fe), we examined the influence of Cl<sup>-</sup> ions on the photoactivity. We conducted photocatalysis of 4-NP at different Cl concentrations (1.2, 12 and 120 mg/L, NaCl was used to add chloride ion). Almost no differences of 4-NP degradation and TOC removal among

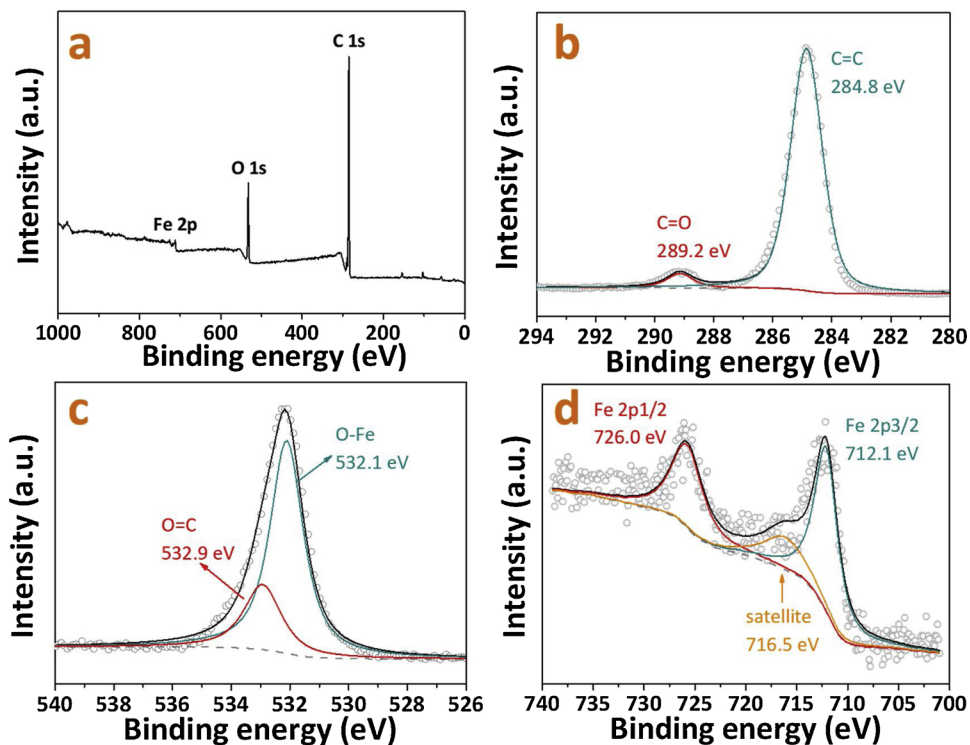


Fig. 3. XPS spectra of MIL-88A(Fe): (a) survey, (b) C 1s, (c) O 1s, (d) Fe 2p.

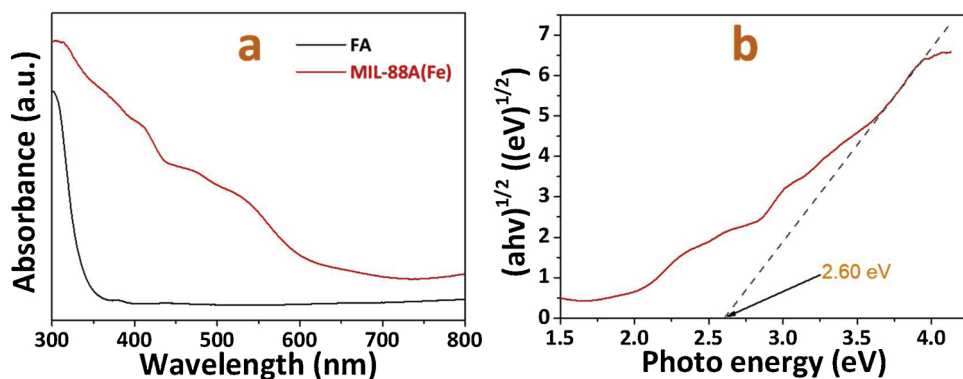


Fig. 4. UV-vis DRS spectra of FA and MIL-88A(Fe) (a); band gap of MIL-88A(Fe) (b).

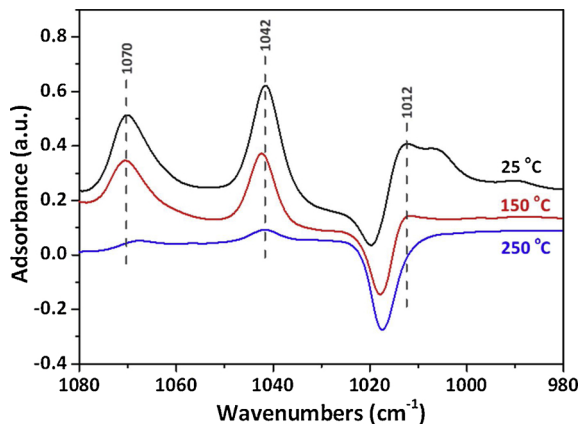


Fig. 5. Py-FTIR spectra of MIL-88A(Fe) at different degassing temperatures (25 °C, 150 °C and 250 °C).

**Table 1**  
Peak area and Lewis acidity of MIL-88A at different degassing temperatures.

Temperature	Peak area	Lewis acid strength	Lewis acidity (mmol/g)
25 °C	2.49	Total	8.53
150 °C	1.52	Medium + Strong	5.21
250 °C	0.23	Strong	0.79

these three systems are observed (Fig. S3). Interestingly, 23.4% of 4-NP (Fig. S4) is destroyed using the visible light irradiation (> 420 nm, 300 W Xe lamp) in photocatalysis system ([MIL-88A(Fe) + Visible light]), indicating the feasibility of coupling ozone and visible light for an enhanced PCO performance. Moreover, the 4-NP degradation efficiencies (Fig. 6a, Table S1) of ozonation alone and catalytic ozonation are found to be 51.4% and 92.9% at 30 min, respectively. The increased efficiencies are attributed to the presence of large amounts of LAS, which plays a key role in the catalytic ozonation. Interestingly, 4-NP is completely removed at 15 min in the PCO system ([MIL-88A(Fe) + UV + Ozone]) (Fig. 6a, Table S1) while only 53.9% removal of 4-NP is achieved in [UV + Ozone] system (Fig. S5). In order to further investigate the degradation performance of different systems, the result is fitted by the pseudo-first-order model, as depicted in Fig. 6b. The kinetic rate constant ( $k$ ) of PCO is  $0.1632 \text{ min}^{-1}$  (Fig. 6d), which is 6.4, 1.9 and 11.3 times higher than those of [UV + Ozone], catalytic ozonation and photocatalysis. The EE/O and energy per m<sup>3</sup> in terms of TOC removal are roughly calculated to be  $27.38 \text{ kW h/m}^3$ -order and  $1.511 \text{ kW h/g}$  (Table S2), which are smaller than those of photocatalysis and catalytic ozonation systems. This indicates that PCO system is more competitive regarding to energy consumption. Most importantly, the TOC removal of the PCO system with MIL-88A(Fe) reaches nearly

75.4%, which is 57.8%, 36.7% and 19.3% greater than those of photocatalysis, catalytic ozonation and their simple combination. This demonstrates the mineralization of 4-NP is enhanced in PCO. In terms of the  $k$  and TOC removal values, a strong synergistic effect can be confirmed in PCO with MIL-88A(Fe) and it may be caused by the conduction band electron capture by the ozone. Besides, the PCO activity and EE/O of MIL-88(Fe) are found to be superior to those of commercial P25 and other Fe-MOFs (Fig. S6 and S7, Table S3).

We also employed ToF-MS to identify the residual chemicals in the treated 4-NP solution. Seven main byproducts were formed from the 4-NP degradation (Fig. S8 and Table S1). The remaining byproducts includes 2-hydroxymalonic acid ( $N_2$  peak), malonic acid ( $N_3$  peak), succinic acid ( $N_4$  peak), oxalic acid ( $N_6$  peak) and acid oxalate ( $N_7$  peak) which were confirmed from the  $m/z$  data (Table. S1) after 30 min. We also recorded the ToF-MS spectra of the samples at reaction times of 5, 60 and 120 min. No 4-NP ( $N_1$  peak) remains after 30 min and it produces five intermediates as mentioned above. Meanwhile, the nitrate ( $N_8$ ) is detected at 30 min, and its content increases with the increasing time while the contents of the other byproducts decrease. Furthermore, the TOC removal can reach to 92% when delaying the reaction time to 120 min, which indicates the residual small acids are also degradable by the MIL-88A(Fe)/PCO system.

It is important to evaluate the pH influence on degradation because of the various pH values in wastewater from different sources. As shown in the Fig. S9, no significant increase or decrease in the degradation efficiency and TOC removal is found in the pH range from 3.0–9.0. This finding demonstrates that the photoresponsive MIL-88A(Fe) with a large amount of LAS gives excellent PCO performance over a wide pH range. This result verifies the value of MIL-88A(Fe) in practical water treatment and wastewater remediation.

To further evaluate the feasibility of MIL-88A(Fe) in real practices, its reusability and stability during catalysis were tested. Almost no discernible decrease in the 4-NP degradation and TOC removal are observed in Fig. 7. Based on the evolution of these two indexes during successive cycles, one can preliminarily conclude that MIL-88A(Fe) has an excellent reusability in PCO processes. In the stability assessment, we employed the ICP-OES technique to monitor the iron leaching concentration during the PCO process. After finishing the reaction at 30 min, about  $0.85 \text{ mg/L}$  of iron is detected in the solution (Fig. S9d) and much lower than the standard ( $2.00 \text{ mg/L}$ ) proposed by the European Union. Since the leached iron may serve as a homogeneous catalyst in the PCO procedure, we studied the influence of iron ions ( $1.00 \text{ mg/L}$ ) on the 4-NP degradation as well as TOC removal. From the inset in Fig. S9d, it can be observed that the degradation efficiency and TOC removal by iron ions are neglectable. In addition, no apparent differences in the XRD patterns (Fig. S10a), FTIR spectra (Fig. S10b) and SEM images (Fig. S10c) are found between the before and after used catalyst. These results demonstrate the practical usability of MIL-88A(Fe).

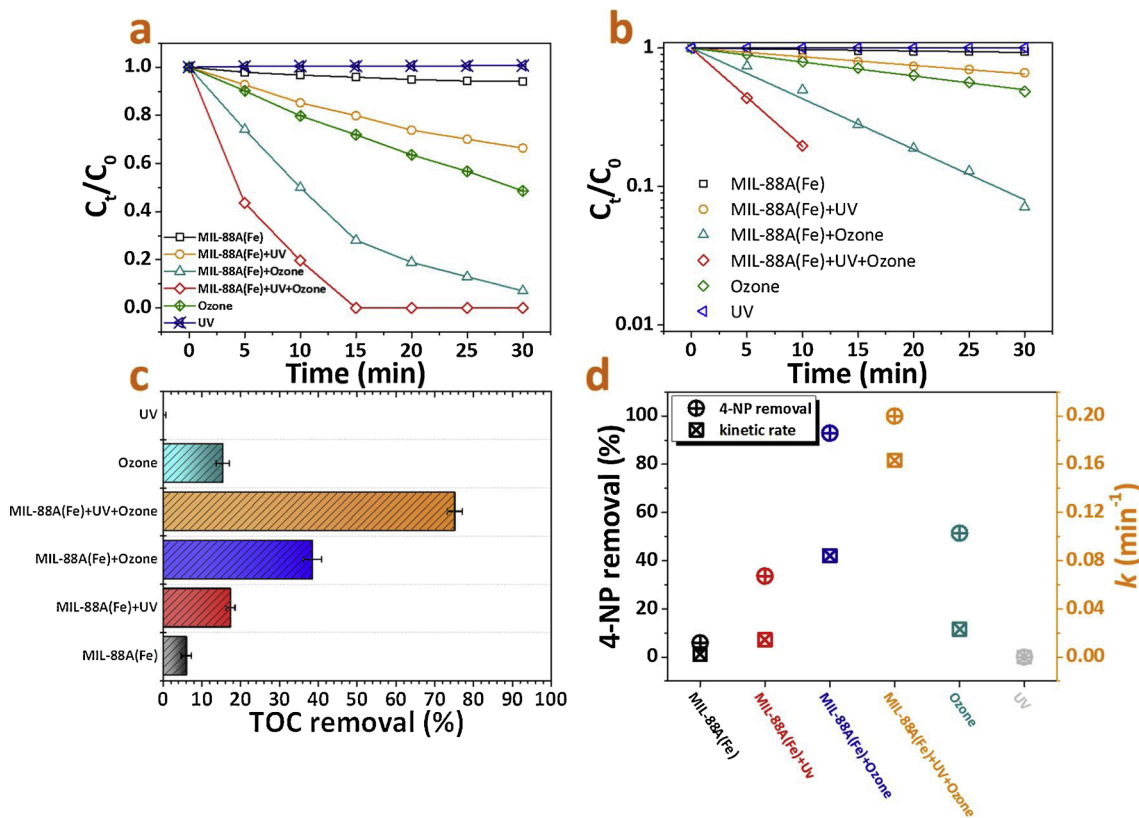


**Fig. 6.** (a) Degradation, (b) pseudo first order plot of 4-NP destruction, (c) TOC removal, (d) 4-NP removal (marked as Circle) and  $k$  values (marked as Square) for the various systems. Reaction conditions: [4-NP] = 100 ppm, [catalyst] = 0.1 g/L, ozone input dosage = 1.5 mg/min-L, UV light intensity =  $3.46 \times 10^{-6}$  Einstiens/L-s, initial pH = 7.0, temperature = 30 °C.

### 3.3. Mechanism investigation

The EPR technique and quenching experiments were employed to study the mechanism of PCO with MIL-88A(Fe) as the catalyst. Fig. 8 describes the EPR spectra of three main ROS ( $\cdot\text{OH}$ ,  $\cdot\text{O}_2^-$ , and  $^1\text{O}_2$ ) and the effect of quenchers (IPA, BQ, and  $\text{NaN}_3$ ) on the 4-NP degradation in the PCO system. No distinct characteristic peaks of DMPO- $\cdot\text{OH}$  and DMPO- $\cdot\text{O}_2^-$  [1,2,8] are detected in the [ozone + UV] system while the EPR spectra of PCO exhibit notable signals (Fig. 8a and 8b). Therefore, the introduction of MIL-88A(Fe) can catalytically generate  $\cdot\text{OH}$  and  $\cdot\text{O}_2^-$  which are definitely absent in the single [ozone + UV] system. From the EPR spectra in Fig. 8c, both [ozone + UV] and PCO systems show the same TEMP/ $^1\text{O}_2$  adducting signals [1,5,9]. However, the intensity of the peaks in the PCO system is much stronger than those in the [ozone + UV] system. These results suggest that  $\cdot\text{OH}$ ,  $\cdot\text{O}_2^-$  and  $^1\text{O}_2$  are the active oxidation species in the PCO process while only  $^1\text{O}_2$  is the

ROS in the [ozone + UV] system. The generation of  $\cdot\text{OH}$  and  $\cdot\text{O}_2^-$  as well as an increased amount of  $^1\text{O}_2$  can facilitate the degradation and mineralization of 4-NP under PCO.

To further verify the contribution of each ROS for 4-NP degradation, quenching experiments using traditional quenchers were conducted. As shown in Fig. 8d, with the addition of quenchers (IPA for  $\cdot\text{OH}$  quenching, BQ for  $\cdot\text{O}_2^-$  quenching and  $\text{NaN}_3$  for  $^1\text{O}_2$ ), all the degradation rates tend to decline. Specifically, only about 25.5% and 28.1% of 4-NP is oxidized in the PCO system when IPA and BQ are individually present, which is much less than the one without adding any quenchers (100%). The degradation efficiency reduces to nearly 60.0% when another trapper ( $\text{NaN}_3$ ) is added into the 4-NP solution. The pseudo-first order  $k$  values of PCO are 0.0087, 0.0108, 0.0297 and 0.1632 min<sup>-1</sup> when IPA, BQ,  $\text{NaN}_3$  and no quenchers are added, respectively (Fig. S11). Therefore, it is proposed that  $\cdot\text{OH}$  and  $\cdot\text{O}_2^-$  play more important roles than  $^1\text{O}_2$  in 4-NP degradation and this supports

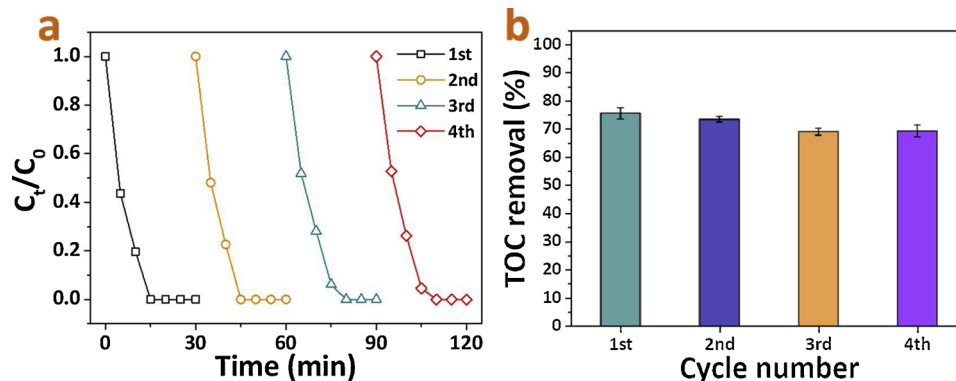


**Fig. 7.** 4-NP degradation (a) and TOC removal (b) in different cycles.

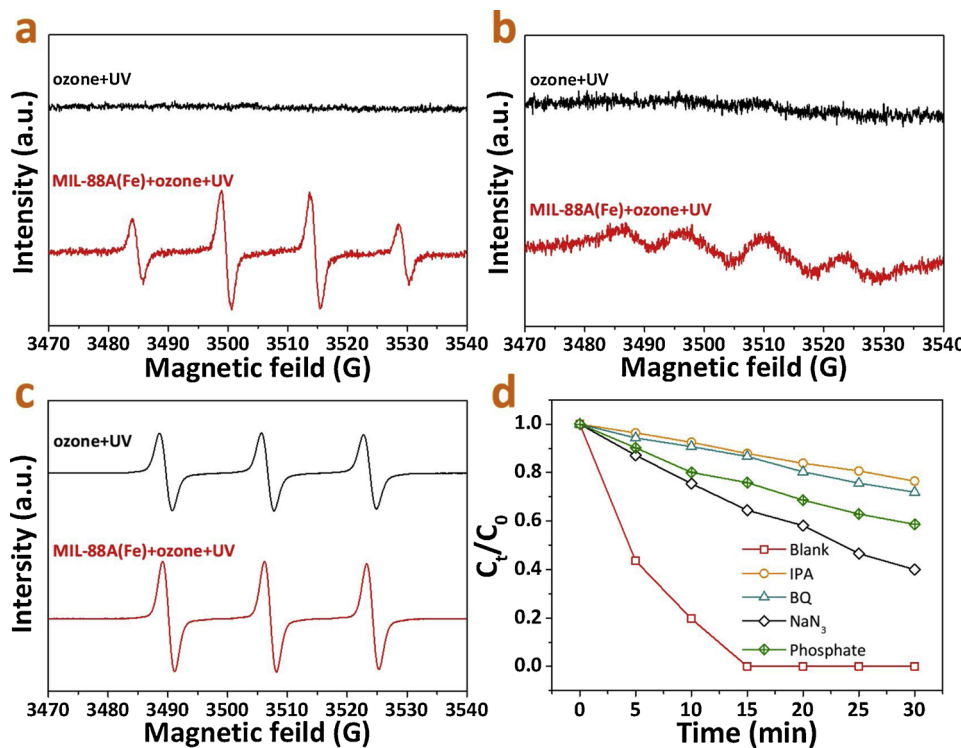


**Fig. 8.** EPR spectra of DMPO/OH (a), DMPO/ $\text{O}_2^-$  (b) and TEPM/ $\text{O}_2$  (c) of simple [ozone + UV] and PCO processes (Testing conditions: [DMPO] = 10 Mm, [TEMP] = 20 mM, [catalyst] = 1.0 g/L, ozone input dosage = 1.5 mg/L-min, UV light intensity =  $3.46 \times 10^6$  Einstiens/L-s, room temperature, reaction time = 5 min); effect of quenchers (IPA, BQ and  $\text{NaN}_3$ ) and phosphate on 4-NP degradation (d) (Reaction conditions: [quencher] = 2.0 g/L, [phosphate] = 2.0 g/L, [4-NP] = 100 ppm, [catalyst] = 0.1 g/L, ozone input dosage = 1.5 mg/L-min, UV light intensity =  $3.46 \times 10^6$  Einstiens/L-s, initial pH = 7.0, temperature = 30 °C).

the EPR findings.

Since the LAS are deemed to be the active sites for ozone adsorption and decomposition, we blocked the Lewis acid sites using phosphate to determine the contribution of catalytic ozonation [52]. As shown in Fig. 8d, a significant decrease (about 58.6%) of the degradation efficiency is recognized in the presence of phosphate (41.4%) with comparison to the PCO system (100%). In particular, the 4-NP removal in the phosphate/PCO system (41.4%) is greater than that of photocatalysis (35.6%). The  $k$  value of the phosphate/PCO system ( $0.0185 \text{ min}^{-1}$ ) is also higher than that of photocatalysis ( $0.0143 \text{ min}^{-1}$ ), possibly because ozone captures conduction band electrons to promote carrier separation and ROS generation. The enhanced carrier separation and ROS generation can trigger a higher 4-NP degradation efficiency and TOC removal.

To prove the above hypothesis and probe the role of ozone, EIS curves and PL spectra were measured to analyze the recombined efficiency of conduction band electrons and valence band holes. Notably, EIS and PL techniques have been widely used to determine the charge carrier separation and recombination efficiency. Fig. 9a and 9b display the Nyquist impedance plots and PL spectra of MIL-88A(Fe) with or without ozone. The charge separation/transfer property is represented

by a semicircle. The arc radius of the sample with ozone ([MIL-88A + Ozone]) is much smaller than that of pristine MIL-88A(Fe), which indicates that the presence of ozone can boost the carrier separation by capturing the conduction band electrons [12,41]. PL spectra have been widely used to verify the recombination of photocarriers because the radiative electron-hole recombination in the photocatalyst generates fluorescence that can be observed by PL emission [16,26,56–58]. The broad PL peaks are assigned to the radiative recombination of photocarriers. The inhibited electron-hole recombination leads to a lower intensity of PL spectrum. The lower PL spectrum intensity of [MIL-88A(Fe) + Ozone] is consistent with the EIS result and further supports the proposed assumption [26,39,41]. In other words, ozone can serve as a strong conduction band electron trapper to suppress the recombination of photocarriers.

To gain a deeper insight into the ROS origin, M-S measurements were performed to study the band structure of MIL-88A(Fe). The band structure resembles that of an n-type semiconductor due to the positive slope of the plot (Fig. 10a) [41]. The flat-band (FB) potential is -0.53 V vs. the saturated calomel electrode (SCE) and equal to -0.29 V vs. the normal hydrogen electrode (NHE). Since the conduction band (CB) is nearly 0.1 V lower than the FB in the case of an n-type semiconductor

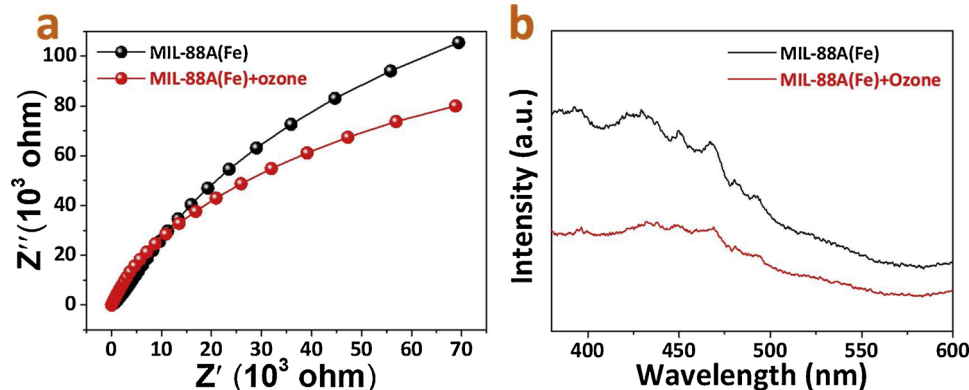


**Fig. 9.** EIS Nyquist impedance plots (a) and PL spectra (b) of MIL-88A(Fe) in the presence or absence of ozone.

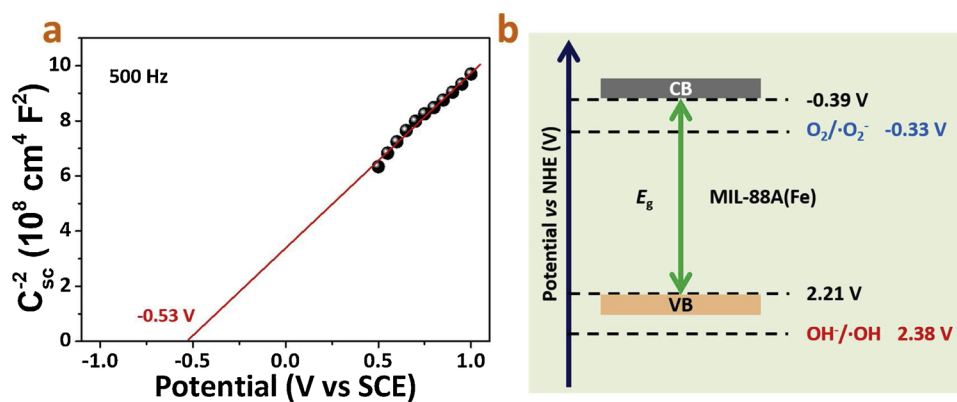
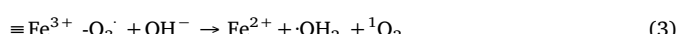
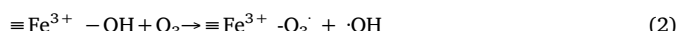


Fig. 10. M-S plots (a) and evaluated energy level illustration (b) of MIL-88A(Fe).

[39], the CB potential is determined to be -0.39 V vs. NHE, as displayed in Fig. 10b. Therefore,  $\cdot\text{O}_2^-$  would be formed to degrade 4-NP in photocatalysis for the higher potential of  $\text{O}_2/\text{O}_2^-$  (-0.33 V) [41]. Combined with the band gap from the UV-vis DRS analysis, the valence band (VB) potential is computed to be 2.21 V. Besides, the VB potential evaluated from valence XPS (Fig. S12a) of MIL-88A(Fe) is about 2.14 eV and further proves its band structure. Thus, MIL-88A(Fe) can not generate  $\cdot\text{OH}$  by the evolution of holes because  $\cdot\text{OH}/\text{OH}^-$  gets a higher potential (2.38 V). We also recorded the EPR spectra of MIL-88A(Fe) under UV (254 nm) to further confirm the ROS involved in photocatalysis. From Fig. S12b, no signals for DMPO-/OH species but quartet peaks with the same intensity for DMPO-/O<sub>2</sub><sup>-</sup> species and triplet peaks with the intensity of 1:2:1 for TEMP/<sup>1</sup>O<sub>2</sub> adducting are discerned, supporting the band structure result.

Consequently, the PCO mechanism of MIL-88A(Fe) is presented in Fig. 11. On the one hand, ozone can be catalytically decomposed into  $\cdot\text{OH}$ ,  $\cdot\text{O}_2^-$ , and <sup>1</sup>O<sub>2</sub> via the surface LAS on MIL-88A(Fe) for 4-NP degradation and mineralization (Eq. (1)–(6)) [3,59]. On the other hand, MIL-88A(Fe) can be triggered to produce conduction band electrons ( $e^-$ ) and holes ( $h^+$ ) in the CB and VB under UV (254 nm) radiation (Eq. (7)). Meanwhile, the conduction band electrons are transferred to ozone to generate more ROS including  $\cdot\text{OH}$ ,  $\cdot\text{O}_2^-$ , and <sup>1</sup>O<sub>2</sub> (Eq. (8)) and enhance photoinduced carrier separation. However,  $\cdot\text{OH}$  is unable to be formed from  $h^+$  due to the low VB potential. Therefore, the excellent

PCO performance of MIL-88A(Fe) derives from its large amount of LAS and strong conduction band electron-capturing ability of ozone.



#### 4. Conclusion

In summary, MIL-88A(Fe) was synthesized with a simple hydrothermal method and a large amount of LAS was created. We tested its performance using 4-NP degradation and mineralization in the PCO process. The degradation and mineralization performance of PCO is much better than those of photocatalysis and catalytic ozonation due to a strong synergistic effect. This effect derives from the conduction band

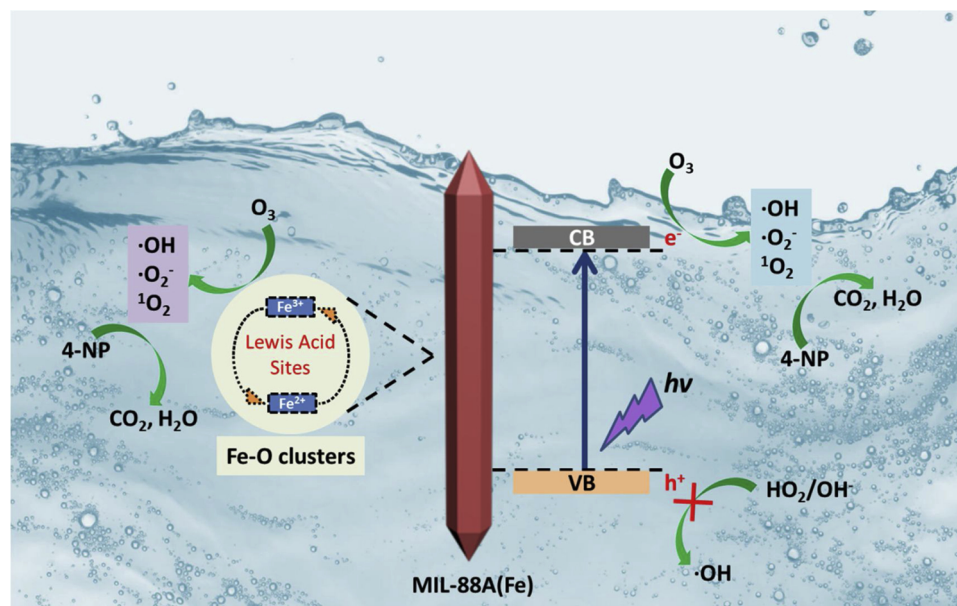


Fig. 11. Proposed PCO mechanism of MIL-88A(Fe) for 4-NP degradation and mineralization.

electron capture by the ozone and this enhances the generation of ROS by reducing charge carrier recombination. In addition, ozone can be catalytically decomposed into ROS at the surface LAS of MIL-88A(Fe) to facilitate 4-NP destruction. Moreover, MIL-88A(Fe) has acceptable stability and reusability in the PCO process and can be used over a wide pH range. This study may pioneer a new path for the environmental application of the MOFs-based AOPs.

## Acknowledgments

We would like to thank the National Natural Science Foundation of China (No. 51703202) and Zhejiang Province (No. NGF18B070005), Sci-Tech Department of Zhejiang Province (No. 2018C03004), Provincial Pivotal Academic Discipline (No. ED2017002, ZYG2017002) and Zhejiang Sci-Tech University (No. 2018-XWLWPY-B-03-06) for their funding support. We also want to thank Dr. Yichen Li, Dr. Tiefeng Xu and Dr. Shishen Zhang for their help with the UV-vis DRS tests, electrochemical experiments and N<sub>2</sub> adsorption-desorption isotherm analyses. The authors also acknowledge the support by the Brook Byers Institute for Sustainable Systems, Hightower Chair and the Georgia Research Alliance at the Georgia Institute of Technology. The authors declare no competing interests.

## Appendix A. Supplementary data

Supplementary material related to this article can be found, in the online version, at doi:<https://doi.org/10.1016/j.apcatb.2019.03.050>.

## References

- [1] T. Yang, J. Peng, Y. Zheng, X. He, Y. Hou, L. Wu, X. Fu, Enhanced photocatalytic ozonation degradation of organic pollutants by ZnO modified TiO<sub>2</sub> nanocomposites, *Appl. Catal. B: Environ.* 221 (2018) 223–234.
- [2] Y. Wang, H. Cao, L. Chen, C. Chen, X. Duan, Y. Xie, W. Song, H. Sun, S. Wang, Tailored synthesis of active reduced graphene oxides from waste graphite: structural defects and pollutant-dependent reactive radicals in aqueous organics decontamination, *Appl. Catal. B: Environ.* 229 (2018) 71–80.
- [3] J. Tang, J. Wang, Metal organic framework with coordinatively unsaturated sites as efficient Fenton-like catalyst for enhanced degradation of sulfamethazine, *Environ. Sci. Technol.* 52 (2018) 5367–5377.
- [4] Y. Wang, H. Cao, C. Chen, Y. Xie, H. Sun, X. Duan, S. Wang, Metal-free catalytic ozonation on surface-engineered graphene: microwave reduction and heteroatom doping, *Chem. Eng. J.* 355 (2019) 118–129.
- [5] S. Zhu, X. Huang, F. Ma, L. Wang, X. Duan, S. Wang, Catalytic removal of aqueous contaminants on N-doped graphitic biochars: inherent roles of adsorption and nonradical mechanisms, *Environ. Sci. Technol.* 52 (2018) 8649–8658.
- [6] Y. Qin, G. Li, Y. Gao, L. Zhang, Y.S. Ok, T. An, Persistent free radicals in carbon-based materials on transformation of refractory organic contaminants (ROCs) in water: a critical review, *Water Res.* 137 (2018) 130–143.
- [7] L. Yuan, J. Shen, P. Yan, Z. Chen, Interface mechanisms of catalytic ozonation with amorphous iron silicate for removal of 4-Chloronitrobenzene in aqueous solution, *Environ. Sci. Technol.* 52 (2018) 1429–1434.
- [8] J. Wang, S. Chen, X. Quan, H. Yu, Fluorine-doped carbon nanotubes as an efficient metal-free catalyst for destruction of organic pollutants in catalytic ozonation, *Chemosphere* 190 (2018) 135–143.
- [9] C. Shan, Y. Xu, M. Hua, M. Gu, Z. Yang, P. Wang, Z. Lu, W. Zhang, B. Pan, Mesoporous Ce-Ti-Zr ternary oxide millispheres for efficient catalytic ozonation in bubble column, *Chem. Eng. J.* 338 (2018) 261–270.
- [10] F. Nawaz, H. Cao, Y. Xie, J. Xiao, Y. Chen, Z.A. Ghazi, Selection of active phase of MnO<sub>2</sub> for catalytic ozonation of 4-nitrophenol, *Chemosphere* 168 (2017) 1457–1466.
- [11] S. Zhang, X. Quan, D. Wang, Catalytic ozonation in arrayed zinc oxide nanotubes as highly efficient mini-column catalyst reactors (MCRs): augmentation of hydroxyl radical exposure, *Environ. Sci. Technol.* 52 (2018) 8701–8711.
- [12] J.D. Xiao, L. Han, J. Luo, S.H. Yu, H.L. Jiang, Integration of plasmonic effects and schottky junctions into metal–organic framework composites: steering charge flow for enhanced visible-light photocatalysis, *Angew. Chem. Int. Ed. Engl.* 57 (2018) 1103–1107.
- [13] L. Jiang, X. Yuan, G. Zeng, Z. Wu, J. Liang, X. Chen, L. Leng, H. Wang, H. Wang, Metal-free efficient photocatalyst for stable visible-light photocatalytic degradation of refractory pollutant, *Appl. Catal. B: Environ.* 221 (2018) 715–725.
- [14] R. Liang, F. Jing, L. Shen, N. Qin, L. Wu, MIL-53(Fe) as a highly efficient bifunctional photocatalyst for the simultaneous reduction of Cr(VI) and oxidation of dyes, *J. Hazard. Mater.* 287 (2015) 364–372.
- [15] C.-C. Wang, J.-R. Li, X.-L. Lv, Y.-Q. Zhang, G. Guo, Photocatalytic organic pollutants degradation in metal–organic frameworks, *Energy Environ. Sci.* 7 (2014) 2831–2867.
- [16] X. Fang, Q. Shang, Y. Wang, L. Jiao, T. Yao, Y. Li, Q. Zhang, Y. Luo, H.L. Jiang, Single Pt atoms confined into a metal–organic framework for efficient photocatalysis, *Adv. Mater.* 30 (2018) 1704303.
- [17] W. Zhang, G. Li, W. Wang, Y. Qin, T. An, X. Xiao, W. Choi, Enhanced photocatalytic mechanism of Ag<sub>3</sub>PO<sub>4</sub> nano-sheets using MS<sub>2</sub> (M = Mo, W)/rGO hybrids as co-catalysts for 4-nitrophenol degradation in water, *Appl. Catal. B: Environ.* 232 (2018) 11–18.
- [18] J. Shi, Y. Kuwahara, M. Wen, M. Navlani-Garcia, K. Mori, T. An, H. Yamashita, Room-temperature and aqueous-phase synthesis of plasmonic molybdenum oxide nanoparticles for visible-light-Enhanced hydrogen generation, *Chem. Asian J.* 11 (2016) 2377–2381.
- [19] S.K. Loeb, P.J.J. Alvarez, J.A. Brame, E.L. Cates, W. Choi, J. Crittenden, D.D. Dionysiou, Q. Li, G. Li-Puma, X. Quan, D.L. Sedlak, T. David Waite, P. Westerhoff, J. H. Kim, The Technology Horizon for Photocatalytic Water Treatment: Sunrise or Sunset?, *Environ. Sci. Technol.*, DOI: 10.1021/acs.est.8b05041.
- [20] Y. Wang, J. Fang, J.C. Crittenden, C. Shen, Novel RGO/alpha-FeOOH supported catalyst for Fenton oxidation of phenol at a wide pH range using solar-light-driven irradiation, *J. Hazard. Mater.* 329 (2017) 321–329.
- [21] N.F.F. Moreira, J.M. Sousa, G. Macedo, A.R. Ribeiro, L. Barreiros, M. Pedrosa, J.L. Faria, M.F.R. Pereira, S. Castro-Silva, M.A. Segundo, C.M. Manaia, O.C. Nunes, A.M.T. Silva, Photocatalytic ozonation of urban wastewater and surface water using immobilized TiO<sub>2</sub> with LEDs: micropollutants, antibiotic resistance genes and estrogenic activity, *Water Res.* 94 (2016) 10–22.
- [22] A.C. Mecha, M.S. Onyango, A. Ochieng, C.J.S. Fourie, M.N.B. Momba, Synergistic effect of UV-vis and solar photocatalytic ozonation on the degradation of phenol in municipal wastewater: a comparative study, *J. Catal.* 341 (2016) 116–125.
- [23] J. Xiao, Y. Xie, H. Cao, Organic pollutants removal in wastewater by heterogeneous photocatalytic ozonation, *Chemosphere* 121 (2015) 1–17.
- [24] J. Qiu, X. Zhang, Y. Feng, X. Zhang, H. Wang, J. Yao, Modified metal–organic frameworks as photocatalysts, *Appl. Catal. B: Environ.* 231 (2018) 317–342.
- [25] X. Liu, Y. Zhou, J. Zhang, L. Tang, L. Luo, G. Zeng, Iron containing metal–organic frameworks: structure, synthesis, and applications in environmental remediation, *ACS Appl. Mat. Interfaces* 9 (2017) 20255–20275.
- [26] L. Shi, L. Yang, H. Zhang, K. Chang, G. Zhao, T. Kako, J. Ye, Implantation of Iron(III) in porphyrin metal organic frameworks for highly improved photocatalytic performance, *Appl. Catal. B: Environ.* 224 (2018) 60–68.
- [27] M. Mon, R. Bruno, J. Ferrando-Soria, D. Armentano, E. Pardo, Metal–organic framework technologies for water remediation: towards a sustainable ecosystem, *J. Mater. Chem. A Mater. Energy Sustain.* 6 (2018) 4912–4947.
- [28] S. Yuan, L. Feng, K. Wang, J. Pang, M. Bosch, C. Lollar, Y. Sun, J. Qin, X. Yang, P. Zhang, Q. Wang, L. Zou, Y. Zhang, L. Zhang, Y. Fang, J. Li, H.C. Zhou, Stable metal–organic frameworks: design, synthesis, and applications, *Adv. Mater.* 30 (2018) 1704303.
- [29] M. Wen, G. Li, H. Liu, J. Chen, T. An, H. Yamashita, Metal–organic framework-based nanomaterials for adsorption and photocatalytic degradation of gaseous pollutants: recent progress and challenges, *Environ. Sci.: Nano*, DOI: 10.1039/c8en01167b.
- [30] K.G. Laurier, F. Vermoortele, R. Ameloot, D.E. De Vos, J. Hofkens, M.B. Roeflaevers, Iron(III)-based metal–organic frameworks as visible light photocatalysts, *J. Am. Chem. Soc.* 135 (2013) 14488–14491.
- [31] F. Jing, R. Liang, J. Xiong, R. Chen, S. Zhang, Y. Li, L. Wu, MIL-68(Fe) as an efficient visible-light-driven photocatalyst for the treatment of a simulated waste-water contain Cr(VI) and Malachite Green, *Appl. Catal. B: Environ.* 206 (2017) 9–15.
- [32] D. Wang, F. Jia, H. Wang, F. Chen, Y. Fang, W. Dong, G. Zeng, X. Li, Q. Yang, X. Yuan, Simultaneously efficient adsorption and photocatalytic degradation of tetracycline by Fe-based MOFs, *J. Colloid Interface Sci.* 519 (2018) 273–284.
- [33] M. Wen, K. Mori, Y. Kuwahara, H. Yamashita, Plasmonic Au@Pd nanoparticles supported on a basic metal–organic framework: synergic boosting of H<sub>2</sub> production from formic acid, *ACS Energy Lett.* 2 (2016) 1–7.
- [34] M. Wen, K. Mori, Y. Kuwahara, T. An, H. Yamashita, Design and architecture of metal organic frameworks for visible light enhanced hydrogen production, *Appl. Catal. B: Environ.* 218 (2017) 555–569.
- [35] M. Wen, K. Mori, Y. Kuwahara, T. An, H. Yamashita, Design of single-site photocatalysts by using metal–Organic frameworks as a matrix, *Chem. Asian J.* 13 (2018) 1767–1779.
- [36] S. Li, S. Sun, H. Wu, C. Wei, Y. Hu, Effects of electron-donating groups on the photocatalytic reaction of MOFs, *Cataly. Sci. Technol.* 8 (2018) 1696–1703.
- [37] L. Shi, T. Wang, H. Zhang, K. Chang, X. Meng, H. Liu, J. Ye, An amine-functionalized Iron(III) metal–Organic framework as efficient visible-light photocatalyst for Cr(VI) reduction, *Adv. Sci. (Weinh)* 2 (2015) 1500006.
- [38] X. Li, Y. Pi, L. Wu, Q. Xia, J. Wu, Z. Li, J. Xiao, Facilitation of the visible light-induced Fenton-like excitation of H<sub>2</sub>O<sub>2</sub> via heterojunction of g-C<sub>3</sub>N<sub>4</sub>/NH<sub>2</sub>-Iron terephthalate metal–organic framework for MB degradation, *Appl. Catal. B: Environ.* 202 (2017) 653–663.
- [39] Y. Gao, S. Li, Y. Li, L. Yao, H. Zhang, Accelerated photocatalytic degradation of organic pollutant over metal–organic framework MIL-53(Fe) under visible LED light mediated by persulfate, *Appl. Catal. B: Environ.* 202 (2017) 165–174.
- [40] D. Yu, M. Wu, Q. Hu, L. Wang, C. Lv, L. Zhang, Iron-based metal–organic frameworks as novel platforms for catalytic ozonation of organic pollutant: efficiency and mechanism, *J. Hazard. Mater.* 367 (2019) 456–464.
- [41] N. Liu, W. Huang, X. Zhang, L. Tang, L. Wang, Y. Wang, M. Wu, Ultrathin graphene oxide encapsulated in uniform MIL-88A(Fe) for enhanced visible light-driven photodegradation of RhB, *Appl. Catal. B: Environ.* 221 (2018) 119–128.
- [42] C.G. Hatchard, C.A. Parker, E.J. Bowen, A new sensitive chemical actinometer - II. Potassium ferrioxalate as a standard chemical actinometer, *Proc. R. Soc. Lond. Ser. A*

- A. Math. Phys. Sci. 235 (1956) 518–536.
- [43] J.C. Crittenden, S. Hu, D.W. Hand, S.A. Green, A kinetic model for H<sub>2</sub>O<sub>2</sub>/UV process in a completely mixed batch reactor, *Water Res.* 33 (1999) 2315–2328.
- [44] P. Horcajada, T. Chalati, C. Serre, B. Gillet, C. Sebrie, T. Baati, J.F. Eubank, D. Heurtaux, P. Clayette, C. Kreuz, J.S. Chang, Y.K. Hwang, V. Marsaud, P.N. Bories, L. Cynober, S. Gil, G. Ferey, P. Couvreur, R. Gref, Porous metal-organic-framework nanoscale carriers as a potential platform for drug delivery and imaging, *Nat. Mater.* 9 (2010) 172–178.
- [45] M. Thommes, K. Kaneko, V. Neimark Alexander, P. Olivier James, F. Rodriguez-Reinoso, J. Rouquerol, S.W. Sing Kenneth, Physisorption of gases, with special reference to the evaluation of surface area and pore size distribution (IUPAC Technical Report), *Pure Appl. Chem.* (2015) 1051.
- [46] R. Liang, S. Luo, F. Jing, L. Shen, N. Qin, L. Wu, A simple strategy for fabrication of Pd@MIL-100(Fe) nanocomposite as a visible-light-driven photocatalyst for the treatment of pharmaceuticals and personal care products (PPCPs), *Appl. Catal. B: Environ.* 176–177 (2015) 240–248.
- [47] S. Yuan, J.S. Qin, C.T. Lollar, H.C. Zhou, Stable metal-organic frameworks with group 4 metals: current status and trends, *ACS Cent. Sci.* 4 (2018) 440–450.
- [48] M.B. Chambers, X. Wang, L. Ellezam, O. Ersen, M. Fontecave, C. Sanchez, L. Rozes, C. Mellot-Draznieks, Maximizing the photocatalytic activity of metal-organic frameworks with aminated-functionalized linkers: substoichiometric effects in MIL-125-NH<sub>2</sub>, *J. Am. Chem. Soc.* 139 (2017) 8222–8228.
- [49] Q. Xia, H. Wang, B. Huang, X. Yuan, J. Zhang, J. Zhang, L. Jiang, T. Xiong, G. Zeng, State-of-the-Art advances and challenges of iron-based metal organic frameworks from attractive features, synthesis to multifunctional applications, *Small* (2018) e1803088.
- [50] G.-T. Vuong, M.-H. Pham, T.-O. Do, Direct synthesis and mechanism of the formation of mixed metal Fe<sub>2</sub>Ni-MIL-88B, *CrystEngComm* 15 (2013) 9694.
- [51] G.T. Vuong, M.H. Pham, T.O. Do, Synthesis and engineering porosity of a mixed metal Fe<sub>2</sub>Ni MIL-88B metal-organic framework, *Dalton Trans.* 42 (2013) 550–557.
- [52] J. Bing, C. Hu, L. Zhang, Enhanced mineralization of pharmaceuticals by surface oxidation over mesoporous γ-Ti-Al<sub>2</sub>O<sub>3</sub> suspension with ozone, *Appl. Catal. B: Environ.* 202 (2017) 118–126.
- [53] C. Volkinger, H. Leclerc, J.-C. Lavalle, T. Loiseau, G. Férey, M. Daturi, A. Vimont, Infrared spectroscopy investigation of the acid sites in the metal–Organic framework aluminum trimesate MIL-100(Al), *J. Phys. Chem. C* 116 (2012) 5710–5719.
- [54] H. Leclerc, A. Vimont, J.C. Lavalle, M. Daturi, A.D. Wiersum, P.L. Llewellyn, P. Horcajada, G. Férey, C. Serre, Infrared study of the influence of reducible iron(III) metal sites on the adsorption of CO, CO<sub>2</sub>, propane, propene and propyne in the mesoporous metal-organic framework MIL-100, *Phys. Chem. Chem. Phys.* 13 (2011) 11748–11756.
- [55] C.A. Emeis, Determination of integrated molar extinction coefficients for infrared absorption bands of pyridine adsorbed on solid acid catalysts, *J. Catal.* 141 (1993) 347–354.
- [56] X. Xu, R. Liu, Y. Cui, X. Liang, C. Lei, S. Meng, Y. Ma, Z. Lei, Z. Yang, PANI/FeUiO-66 nanohybrids with enhanced visible-light promoted photocatalytic activity for the selectively aerobic oxidation of aromatic alcohols, *Appl. Catal. B: Environ.* 210 (2017) 484–494.
- [57] S. Wang, B.Y. Guan, X.W.D. Lou, Construction of ZnIn<sub>2</sub>S<sub>4</sub>-In<sub>2</sub>O<sub>3</sub> hierarchical tubular heterostructures for efficient CO<sub>2</sub> photoreduction, *J. Am. Chem. Soc.* 140 (2018) 5037–5040.
- [58] Z. Yang, X. Xu, X. Liang, C. Lei, Y. Cui, W. Wu, Y. Yang, Z. Zhang, Z. Lei, Construction of heterostructured MIL-125/Ag/g-C<sub>3</sub>N<sub>4</sub> nanocomposite as an efficient bifunctional visible light photocatalyst for the organic oxidation and reduction reactions, *Appl. Catal. B: Environ.* 205 (2017) 42–54.
- [59] J. Bing, C. Hu, Y. Nie, M. Yang, J. Qu, Mechanism of catalytic ozonation in Fe<sub>2</sub>O<sub>3</sub>/Al<sub>2</sub>O<sub>3</sub>@SBA-15 aqueous suspension for destruction of ibuprofen, *Environ. Sci. Technol.* 49 (2015) 1690–1697.